

Electronic Supplementary Information

Determining the photostability of avobenzone in sunscreen formulation models using ultrafast spectroscopy

E. L. Holt^{a,b}, N. d. N. Rodrigues^{a,c}, J. Cebrián^c, V. G. Stavros^{a*}

^a Department of Chemistry, University of Warwick, Gibbet Hill Road, Coventry, CV4 7AL, United Kingdom

^b Molecular Analytical Science Centre for Doctoral Training, Senate House, University of Warwick, Coventry, CV4 7AL, United Kingdom

^c Lubrizol Life Science Beauty, C/Isaac Peral 17-Pol. Industrial Cami Ral, 08850 Gava, Spain

*Correspondence: v.stavros@warwick.ac.uk

Supplementary Methods

(a) Instrument response

To estimate the instrument response function (IRF) of our TEAS setup, solvent-only scans of each solvent were taken under the same conditions as the sample, for time delays between -1 ps and 1 ps. A representative slice at ~ 380 nm was taken across all time delays and the resulting transients were fitted with a Gaussian function, shown in Equation 1. In this equation, A denotes the amplitude of the fitted curve; t_0 is the fitted time zero, indicating the centre of the curve where the peak amplitude occurs; σ is the standard deviation of the curve and finally, s is a variable that allows for any signal offset. In practice, t_0 is the exact time where the pump and probe meet the sample at the same time.

$$f(t) = A \exp\left(-\frac{(t-t_0)^2}{2\sigma^2}\right) + s \quad (1)$$

The value of σ is converted to the full width at half maximum (FWHM) value to extract the IRF, by multiplying by the scaling factor $2\sqrt{2\ln 2}$. After scaling, the extracted IRF lifetimes are ~ 140 fs in ethanol and ~ 80 fs in cyclohexane. The raw data and the fitted Gaussian function are shown in Fig. S1. At the selected wavelength, it was not possible to attain any signal from the solvent alone from either of the emollients, diisopropyl adipate and lauryl lactate. However, the upper bound of these lifetimes (140 fs) can be considered a good estimate for the IRF in emollient.

(b) Computational methods

All calculations were performed using the NWChem software package.¹ Density functional theory (DFT) geometry optimisations for the *chelated enol* and *diketo* structures of avobenzene (see Fig. 1) were carried out to determine the most stable, lowest energy conformations in the ground state. These calculations were conducted in implicitly modelled ethanol and cyclohexane, using the conductor-like screening model (COSMO, with SMD) built into NWChem.^{2, 3} The relaxation of the initial *enol* and *diketo* structures of avobenzene was initially carried out using DFT at the PBE/6-31g* level of theory. This initial structure was then further optimized either by improving the functional to PBE0 or improving the basis set to 6-311++g**, before arriving at the final structure, which was calculated at the PBE0/6-311++g** level of theory. Once these optimised structures were attained, time-dependent DFT (TD-DFT) was carried out to attain the vertical excitation energies of the singlet (S_n) and triplet (T_n) states of each species in both solvents using the same COSMO model. The vertical excitation energies of the five lowest energy singlet and triplet states were calculated using these optimised structures using TD-DFT at the PBE0/6-311++g** level of theory. The state characters were also calculated during these TD-DFT calculations and assigned manually. For additional confirmation of the T_1 state energy, a Δ SCF methodology was also used.⁴ The triplet single point energy for the Δ SCF method was calculated at the PBE0/6-311++g** level of theory. For this, the multiplicity was set to three on each of the optimised ground state structures; the single point energy was then compared to the ground state single point energy.

(c) SPF testing

The SPF and UVA-PF values for the five oil phase samples, prepared as described in the main manuscript were measured. Square poly(methyl methacrylate) (PMMA) plates of 5 cm by 5 cm (25 cm²), with a textured surface on one side and smooth on the other, were cleaned with deionized water and left to dry in a temperature controlled chamber at 25°C for at least two hours, until they were ready for use. Approximately 15 mg of sample was placed on the plates in a 3 x 3 square grid pattern. The samples were then applied by rubbing the samples onto each plate with a gloved finger (nitrile gloves), first in rotative motions and then with swift back and forth motions between opposite edges of the square plate, to achieve an even distribution of sample on the plate. After application, the sample coated PMMA plates were left to rest in the HD-Thermaster at 25°C for 30 minutes before testing. A blank plate was prepared in a similar fashion, using 15 mg of glycerin applied in a 3 x 3-point grid.

The SPF and UVA-PF studies were carried out using a LabSphere UV-2000 ultraviolet (UV) transmittance analyser (LabSphere, Inc.). The SPF and UVA-PF values for each plate are calculated based on an average of readings from 5 different points on the plate. The final values presented in Table 2 in the main manuscript are an average of 3 plates for each oil phase sample. Each plate was analysed before and after irradiation with a SUNTEST CPS+ (III) solar simulator (Atlas Material Testing Solutions). This solar simulator delivers 550 W/m² over the 300 – 800 nm wavelength range, and the irradiation was carried out for 3 hours and 36 minutes, equating to a radiation dose of approximately 7130 kJ/m², comparable with that delivered for the photostability measurements presented in the main manuscript.

Supplementary Discussion

(a) Review on skin surface temperature

Skin surface temperature (SST) is affected by factors such as climate,^{5,6} humidity,⁷ exercise,^{8,9} and wound healing,¹⁰ all of which may affect the efficacy of a sunscreen. Commonly, determination of mean SST (T_s) requires the summation of a finite number (n) of local skin temperatures (t_i), multiplied by a weighting factor (w_i),^{11,12} which is usually the fraction of the total body area each local measurement accounts for.¹² This can be notated according to Equation 2.

$$T_s = \sum_{i=1}^n w_i \cdot t_i \quad (2)$$

However, establishing reliable parameters to substitute into Equation 2 presents challenges, and indicates that a range of temperatures could be recommended for simulating human SST during the collection of ultrafast spectra. One study investigating the effects of exercise on mean SST, by de Andrade Fernandes *et al.*,⁹ found that two methods of measuring t_i , (thermocouple and infrared thermography) offered statistically significant differences on the value of T_s . Furthermore, their results could have been dependent on factors including types of exercise, weather conditions and whether subjects are male or female.

In addition to ascertaining reliable t_i measurements, the optimum weighting factors for n sites ($3 \leq n \leq 17$) have also been investigated; an extensive review of these is provided by Liu *et al.*¹² The number and location of local measurement sites, including the corresponding w_i , are not standardised. This lack of standardisation creates a source of inconsistency between results found in mean SST studies. In the publication by Liu *et al.*,⁵ SST measurements were plotted

individually for typical areas that sunscreen is applied to, such as the face and arms. On the face, the SST was between 35 and 38°C (in a climatic chamber at temperatures between 26 and 38°C), whereas on the arms, the range under equivalent conditions was 32 and 35°C. The mean SST found in this study (measured using thermocouples) was 33 to 36°C. Notably, the mean SST results from comparable ambient conditions (26, 30 and 34°C) between studies by Liu *et al.*⁵ and Atmaca and Yigit⁷ are in close agreement with one another ($\pm 0.4^\circ\text{C}$), which increases confidence in the accuracy of this temperature range.

It is normal for SST to be below that of core body temperature ($\sim 37^\circ\text{C}$),¹³ however some studies have shown that this temperature can also be exceeded. González-Alonso *et al.*¹⁴ found that the maximum T_s when subjects performed exercise under very extreme conditions ($\sim 40^\circ\text{C}$) was 38°C. Local SSTs have also been found to exceed the human core body temperature; as mentioned previously, the local SST of facial skin peaked at 38°C in the study by Liu *et al.*⁵ Another scenario where localised increase in SST occurs is during the healing of a wound, which can cause the temperature of the skin surrounding it (the periwound) to increase beyond 37°C.^{10, 13}

In conclusion, the temperature of the CaF₂ substrate and sample mixture should be heated to above room temperature to be representative of human SST. Any temperature within the range 32 to 38°C is justifiable in the literature for sunscreen applications. If experiments were to be focused on one temperature alone, important effects of temperature on the photochemical properties of sunscreen molecules may be missed.

Supplementary Figures

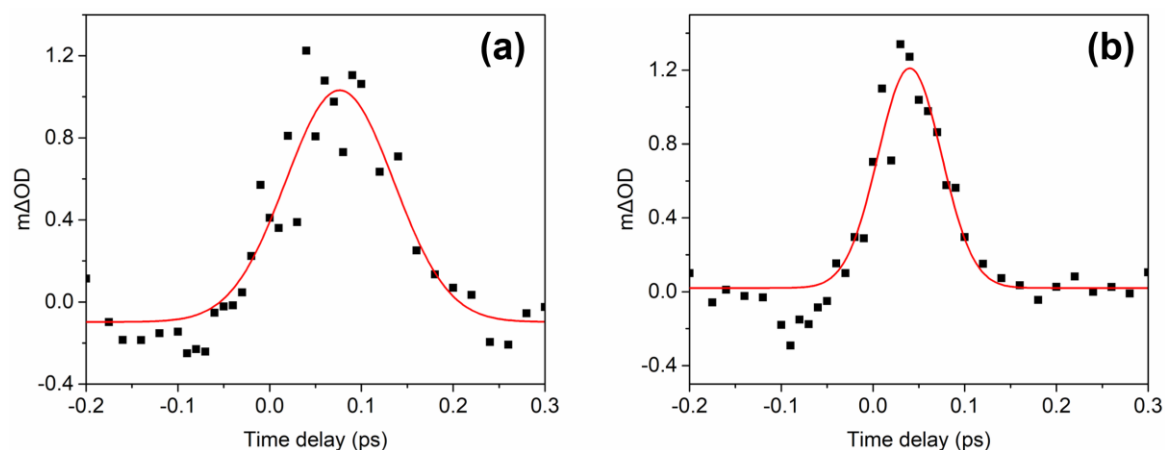


Figure S1: Instrument response functions in (a) ethanol (378 nm probe) and (b) cyclohexane (381 nm probe), when pumped at 350 nm, through 25 μm path length, without heating. The full-width half maximum was calculated to be ~ 140 fs in (a) and ~ 80 fs in (b).

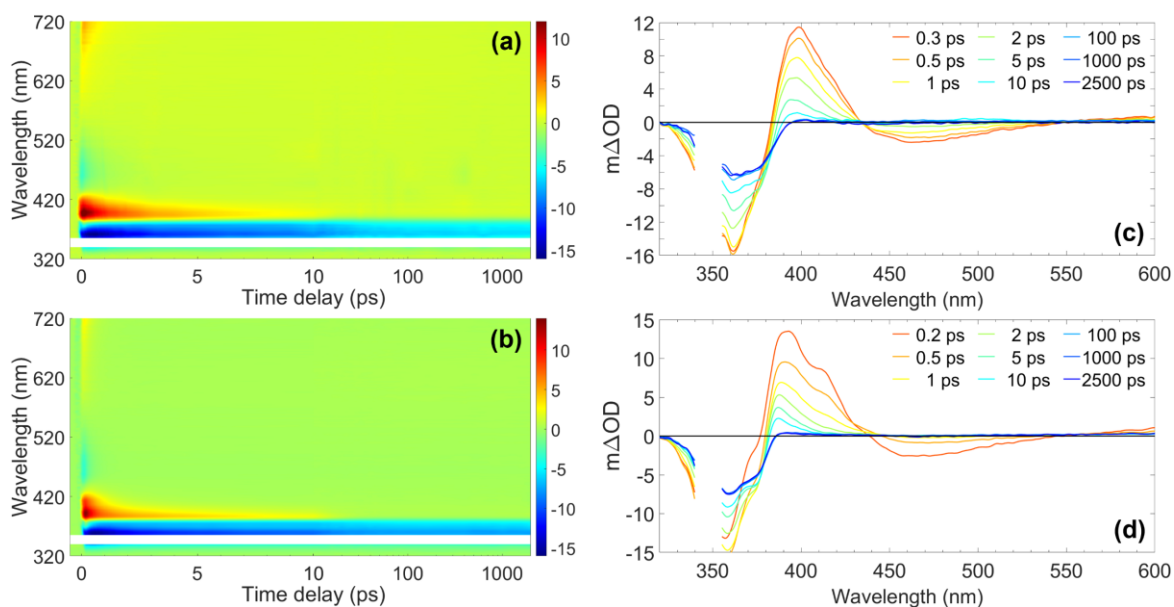


Figure S2: (Left) False colour heat maps showing all transient absorption spectra (TAS) of ~ 10 mM avobenzene photoexcited at approximately 350 nm in (a) ethanol and (b) cyclohexane with no heat applied. (Right) TAS at selected pump-probe time delays for avobenzene in (c) ethanol and (d) cyclohexane with no heat applied. These (right) plots are attained by taking vertical slices through the corresponding false colour heat maps at the given time delay and are presented using the same scale as the corresponding heat map. The region between 340 and 355 nm has been removed due to the pump laser pulse interfering with the data.

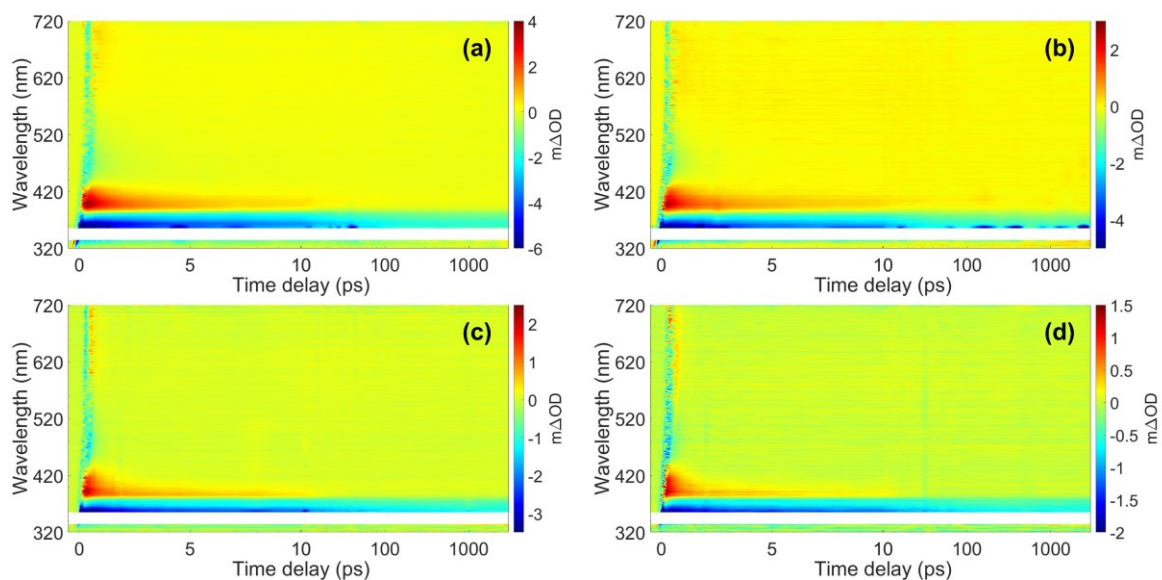


Figure S3: False colour heat maps (not chirp corrected) showing all transient absorption spectra (TAS) of ~ 1 mM avobenzene photoexcited at around 350 nm (a) in ethanol with no heat applied; (b) in ethanol with the sample cell heated to 35°C; (c) in cyclohexane with no heat applied and (d) in cyclohexane with the sample cell heated to 35°C. The region between 340 and 355 nm has been removed due to the pump laser pulse interfering with the data.

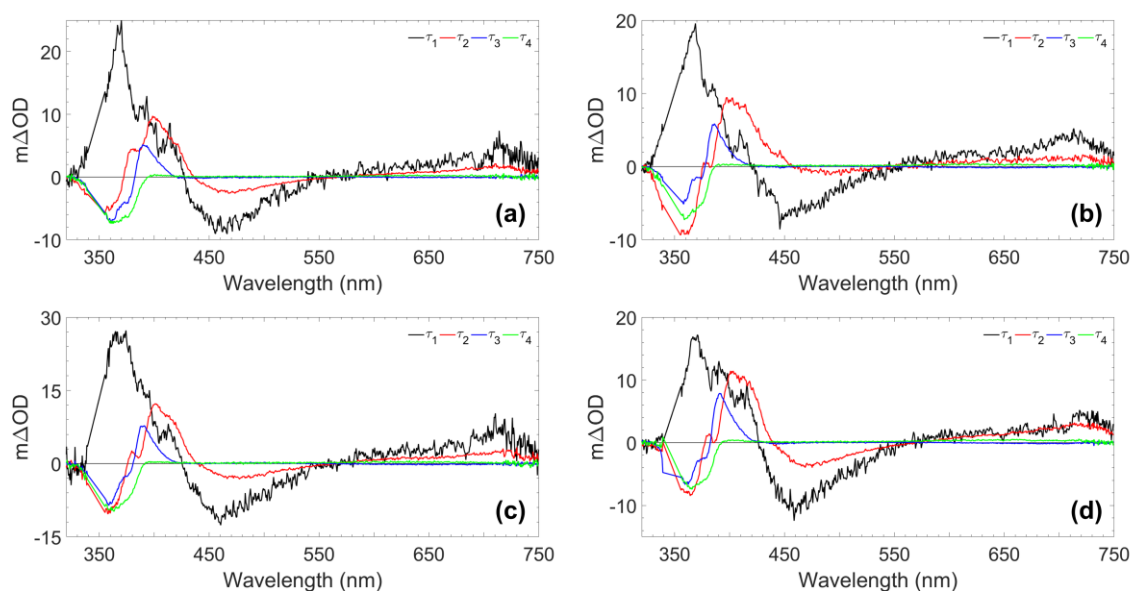


Figure S4: Decay associated spectra (DAS) for heated ~ 10 mM avobenzene solutions in (a) ethanol, (b) cyclohexane, (c) DIA and (d) LL, following photoexcitation at ~ 350 nm. These were obtained by using a parallel global kinetic fit model. The associated time constants can be found in Table 1 of the main manuscript. The values in the 340 – 355 nm region have been linearly interpolated.

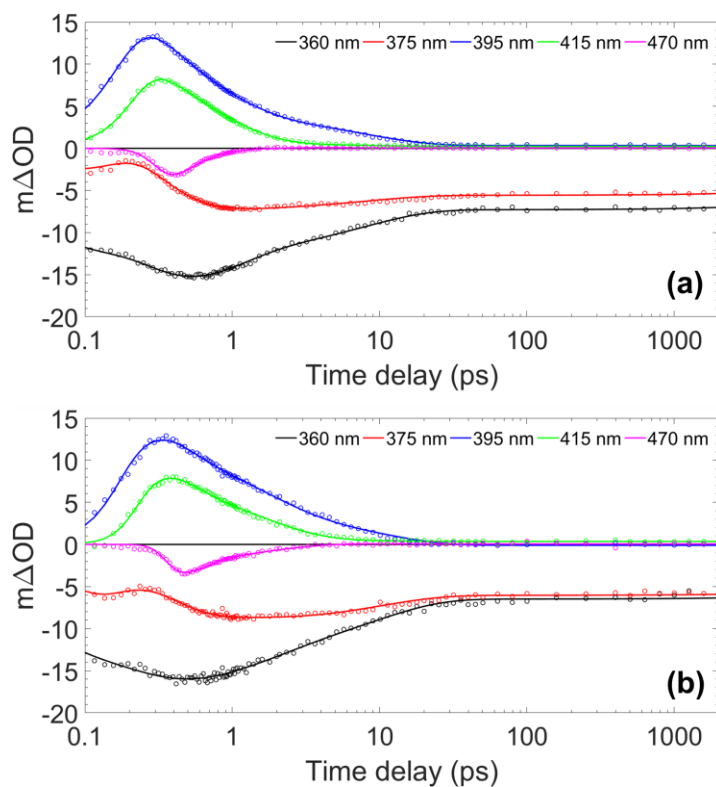


Figure S5: Lineouts to show spectral features at specific probe wavelengths for ~ 10 mM avobenzene in (a) cyclohexane and (b) ethanol with no heat applied. The circles denote the raw datapoints and the solid line in each case is the fit attained using a parallel kinetic model (time constants resulting from this fitting are shown in Table S3). The features at 360 nm and 375 nm are ground-state bleach features, 395 nm and 415 nm are excited-state absorption features and 470 nm is stimulated emission (see main manuscript for further details and discussion). The time delay axis is presented on a logarithmic scale. Time delays prior to 0.1 ps are presented on a linear scale in Fig. S6.

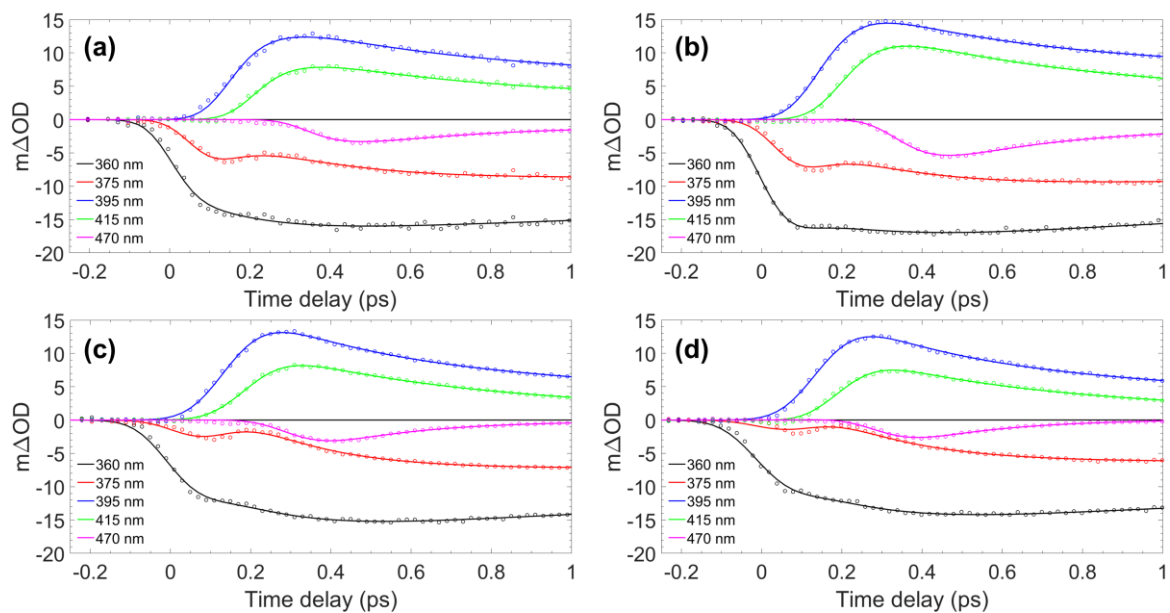


Figure S6: Lineouts prior to 1 ps showing spectral features at specific probe wavelengths for avobenzone photoexcited at around 350 nm (a) in ethanol with no heat applied; (b) in ethanol with the sample cell heated to 35°C; (c) in cyclohexane with no heat applied and (d) in cyclohexane with the sample cell heated to 35°C. The circles denote the raw datapoints and the solid line in each case is the fit attained using a parallel kinetic model.

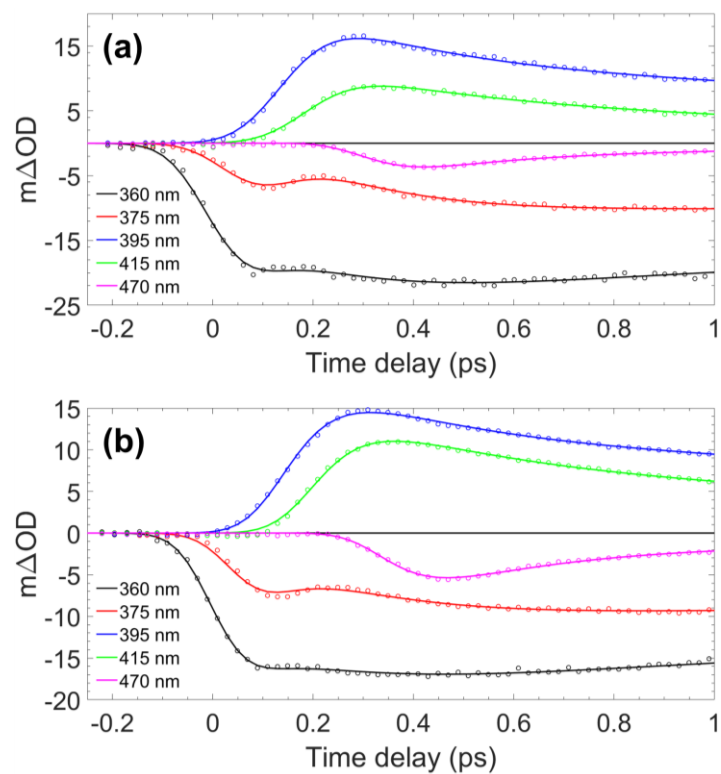


Figure S7: Lineouts prior to 1 ps showing spectral features at specific probe wavelengths for ~ 10 mM avobenzone photoexcited at around 350 nm and heated to $\sim 35^\circ\text{C}$ in (a) diisopropyl adipate (DIA) and (b) lauryl lactate (LL). The circles denote the raw datapoints and the solid line in each case is the fit attained using a parallel model.

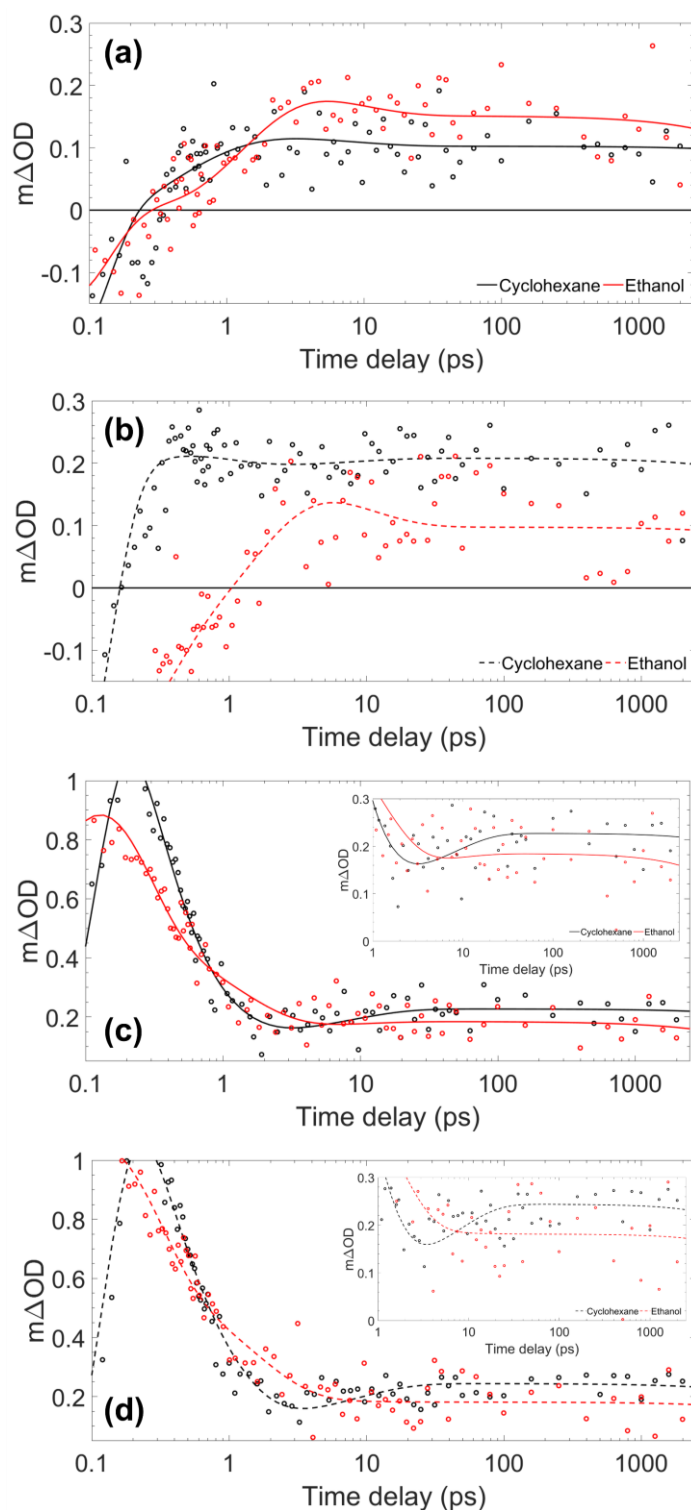


Figure S8: Lineouts to show offset feature at (a), (b) 550 nm and (c), (d) 600 nm for ~ 10 mM avobenzene in (red) ethanol and (black) cyclohexane photoexcited at 350 nm under heating to $\sim 35^\circ\text{C}$ (solid lines) and at room temperature (dotted lines). The circles denote the raw datapoints and the solid/dotted line in each case is the fit attained using a parallel model. The inset figure at 600 nm is a zoom-in of the data between the $m\Delta OD$ values of 0 and 0.3. The time delay axis is presented on a logarithmic scale.

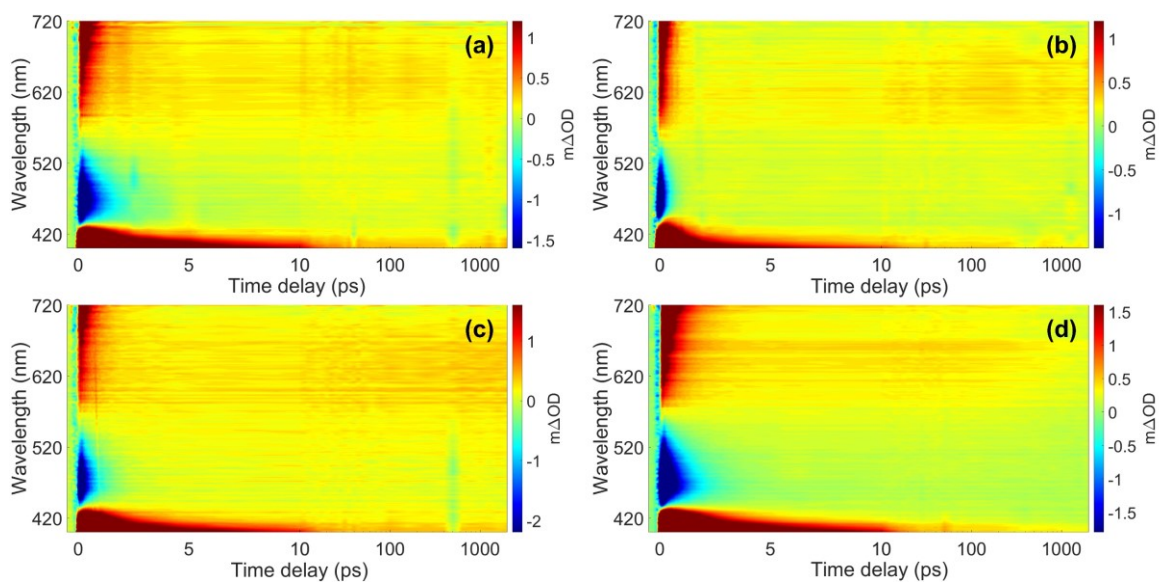


Figure S9: False colour heat maps showing all transient absorption spectra (TAS) of ~ 10 mM avobenzene photoexcited at approximately 350 nm heated to 35°C in (a) ethanol, (b) cyclohexane, (c) diisopropyl adipate (DIA) and (d) lauryl lactate (LL), between the probe wavelengths of 400 – 720 nm. The $m\Delta OD$ scale is 10-fold reduced compared to those presented in Fig. 2 in the main manuscript, to highlight the weaker features.

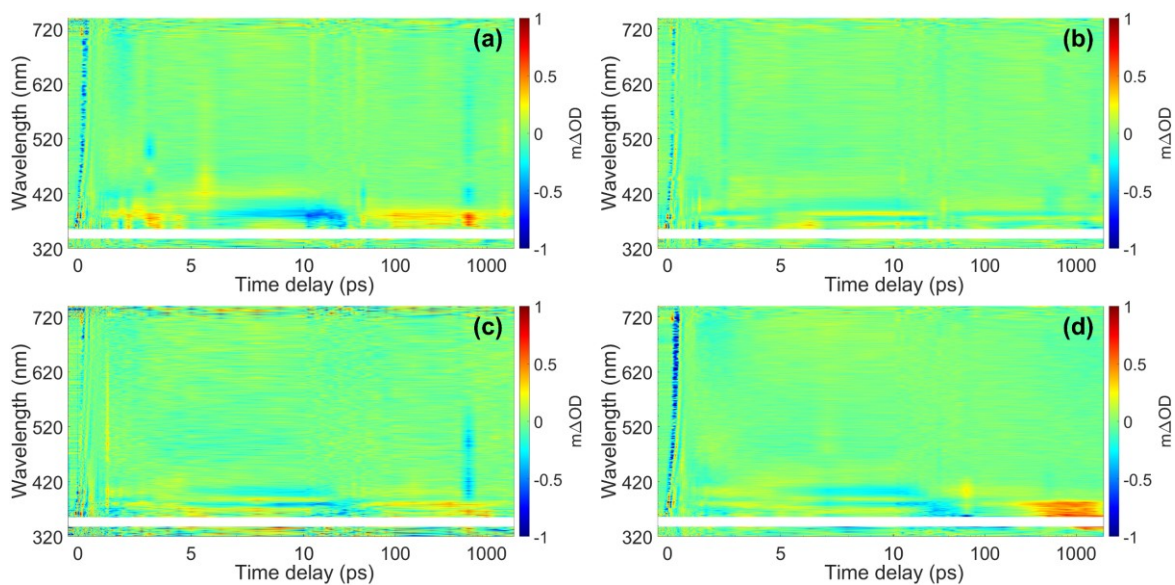


Figure S10: False colour heat maps showing the residuals attained from the parallel fitting procedure of ~ 10 mM avobenzene, photoexcited at approximately 350 nm and heated to 35°C in (a) ethanol, (b) cyclohexane, (c) diisopropyl adipate (DIA) and (d) lauryl lactate (LL).

Supplementary Tables

Table S1: Breakdown of the ingredients in the oil phases, per 25 g batch, tested for SPF and UVA-PF performance following irradiation.

Test	Raw Material	Sample 1	Sample 2
		Mass (g)	Mass (g)
Different emollients	Diisopropyl adipate	10	-
	Lauryl lactate	-	10
	Avobenzone	2.2	2.2
	Ethylhexyl methoxycinnamate	5.5	5.5
	Octocrylene	7.3	7.3
Different concentrations	Raw Material	Sample 3	Sample 4
		Mass (g)	Mass (g)
	Diisopropyl adipate	22	23.5
	Avobenzone	0.44	0.22
	Ethylhexyl methoxycinnamate	1.1	0.55
Octocrylene	1.46	0.73	
Different proportions	Raw Material	Sample 5	
		Mass (g)	
	Diisopropyl adipate	10	
	Avobenzone	2.2	
	Ethylhexyl methoxycinnamate	7.3	
Octocrylene	5.5		

Table S2: Amount of oil phase sample deposited onto each plate, along with amount after application and calculated final coverage for each PMMA plate analysed.

Sample	Plate number	Initial weight (mg)	Final weight (mg)	Final coverage (mg/cm ²)
1	1	14.8	9.6	0.384
	2	15.7	10.2	0.408
	3	15.6	9.3	0.372
Average		15.4	9.7	0.388
Standard Deviation		0.4	0.4	0.01
2	1	14.7	10.4	0.416
	2	14.8	9.6	0.384
	3	14.8	10.6	0.424
Average		14.8	10.2	0.408
Standard Deviation		0.05	0.4	0.02
3	1	15.3	10.3	0.412
	2	14.8	10.2	0.408
	3	14.9	10.9	0.436
Average		15.0	10.5	0.419
Standard Deviation		0.2	0.3	0.01
4	1	14.9	10.2	0.408
	2	15.2	10.6	0.424
	3	14.5	10.0	0.400
Average		14.9	10.3	0.411
Standard Deviation		0.3	0.3	0.01
5	1	14.4	10.7	0.428
	2	14.6	10.2	0.408
	3	15.0	10.2	0.408
Average		14.7	10.4	0.415
Standard Deviation		0.3	0.2	0.01

Table S3: Extracted TEAS time constants for two unheated ~10 mM avobenzene solutions, following photoexcitation at ~350 nm, obtained by using a parallel global kinetic fit model. The error presented for τ_1 is the estimated instrument response (presented in Fig. S1); the errors presented for $\tau_{2,3}$ are those provided by the software package. The quality of the fit is demonstrated in Fig. S5.

Time constant	Ethanol †	Cyclohexane
τ_1 (fs)	160 ± 140	210 ± 80
τ_2 (ps)	1.5 ± 0.1	0.74 ± 0.08
τ_3 (ps)	9.3 ± 0.1	8.0 ± 0.1
τ_4 (ns)	> 2.5*	> 2.5*

* Outside the time-window of the instrument

† During fitting τ_4 was arbitrarily fixed to 50 ns to aid convergence.

Table S4: Predicted singlet and triplet excited state vertical excitation energies (in nm) for the optimised ground-state geometry of avobenzene in its *chelated enol* and *diketo* forms. The energies, and state characters indicated in brackets, were calculated using TD-DFT at the PBE0/6-311++g** level of theory. The optimised ground-state structure, calculated using DFT using the methods detailed in the main manuscript, is also shown.

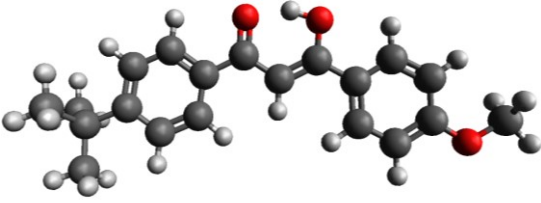
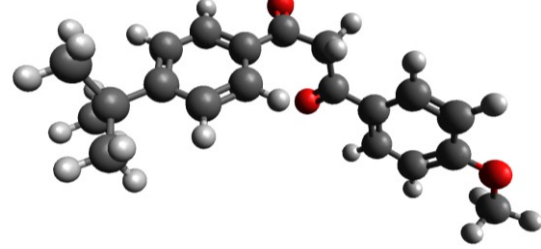
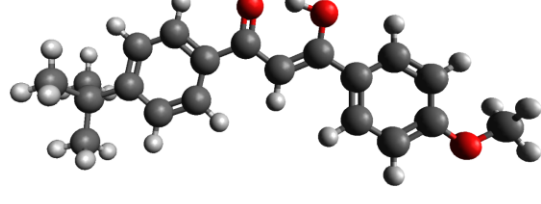
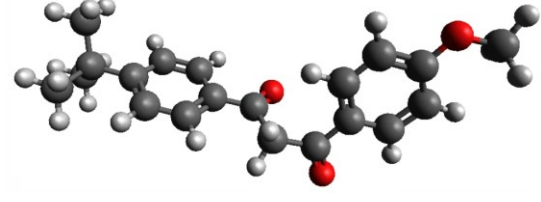
Ethanol				
<i>Chelated enol</i>	Singlets		Triplets	
	S_1 ($\pi\pi^*$)	346	T_1 ($\pi\pi^*$)	500
	S_2 ($n\pi^*$)	309	T_2 ($\pi\pi^*$)	390
	S_3 ($\pi\pi^*$)	283	T_3 ($\pi\pi^*$)	360
	S_4 ($\pi\pi^*$)	281	T_4 ($n\pi^*$)	337
	S_5 ($\pi\pi^*$)	273	T_5 ($\pi\pi^*$)	320
<i>Diketo</i>	Singlets		Triplets	
	S_1 ($n\pi^*$)	313	T_1 ($\pi\pi^*$)	404
	S_2 ($n\pi^*$)	298	T_2 ($\pi\pi^*$)	396
	S_3 ($\pi\pi^*$)	284	T_3 ($n\pi^*$)	360
	S_4 ($\pi\pi^*$)	272	T_4 ($n\pi^*$)	339
	S_5 ($\pi\pi^*$)	266	T_5 ($\pi\pi^*$)	317
Cyclohexane				
<i>Chelated enol</i>	Singlets		Triplets	
	S_1 ($\pi\pi^*$)	337	T_1 ($\pi\pi^*$)	490
	S_2 ($n\pi^*$)	314	T_2 ($\pi\pi^*$)	387
	S_3 ($\pi\pi^*$)	276	T_3 ($\pi\pi^*$)	359
	S_4 ($\pi\pi^*$)	275	T_4 ($n\pi^*$)	344
	S_5 ($\pi\pi^*$)	267	T_5 ($\pi\pi^*$)	313
<i>Diketo</i>	Singlets		Triplets	
	S_1 ($n\pi^*$)	317	T_1 ($\pi\pi^*$)	402
	S_2 ($n\pi^*$)	315	T_2 ($\pi\pi^*$)	386
	S_3 ($\pi\pi^*$)	284	T_3 ($n\pi^*$)	367
	S_4 ($\pi\pi^*$)	266	T_4 ($n\pi^*$)	365
	S_5 ($n\pi^*$)	262	T_5 ($\pi\pi^*$)	305

Table S5: Calculated Δ SCF values for the optimised ground-state geometries of avobenzene (*chelated enol* and *diketo* forms), calculated using DFT at the PBE0/6-311++g** level of theory. To model the triplet state, the ground state geometry was used with the multiplicity set to 3.

<i>Chelated enol</i>		
Solvent	Energy (eV)	Wavelength (nm)
Ethanol	2.6258	472
Cyclohexane	2.6924	460
<i>Diketo</i>		
Solvent	Energy (eV)	Wavelength (nm)
Ethanol	3.2439	382
Cyclohexane	3.3539	370

References

1. M. Valiev, E. J. Bylaska, N. Govind, K. Kowalski, T. P. Straatsma, H. J. Van Dam, D. Wang, J. Nieplocha, E. Apra and T. L. Windus, *Computer Physics Communications*, 2010, **181**, 1477-1489.
2. A. Klamt and G. Schüürmann, *Journal of the Chemical Society, Perkin Transactions 2*, 1993, 799-805.
3. A. V. Marenich, C. J. Cramer and D. G. Truhlar, *The Journal of Physical Chemistry B*, 2009, **113**, 6378-6396.
4. R. J. Charlton, R. M. Fogarty, S. Bogatko, T. J. Zuehlsdorff, N. D. M. Hine, M. Heeney, A. P. Horsfield and P. D. Haynes, *The Journal of Chemical Physics*, 2018, **148**, 104108.
5. Y. Liu, L. Wang, J. Liu and Y. Di, *Journal of Thermal Biology*, 2013, **38**, 440-448.
6. H. Liu, J. Liao, D. Yang, X. Du, P. Hu, Y. Yang and B. Li, *Building and Environment*, 2014, **73**, 232-238.
7. I. Atmaca and A. Yigit, *Journal of Thermal Biology*, 2006, **31**, 442-452.
8. G. Tanda, *Experimental Thermal and Fluid Science*, 2016, **71**, 103-113.
9. A. de Andrade Fernandes, P. R. dos Santos Amorim, C. J. Brito, A. G. de Moura, D. G. Moreira, C. M. A. Costa, M. Sillero-Quintana and J. C. B. Marins, *Physiological Measurement*, 2014, **35**, 189.
10. M. Fierheller and R. G. Sibbald, *Advances in Skin and Wound Care*, 2010, **23**, 369-379.

11. J. Choi, K. Miki, S. Sagawa and K. Shiraki, *International Journal of Biometeorology*, 1997, **41**, 68-75.
12. W. Liu, Z. Lian, Q. Deng and Y. Liu, *Building and Environment*, 2011, **46**, 478-488.
13. Ç. Yağmur, M. S. Engin and R. Ogawa, *Medical Hypotheses*, 2016, **97**, 4-6.
14. J. González-Alonso, C. Teller, S. L. Andersen, F. B. Jensen, T. Hyldig and B. Nielsen, *Journal of Applied Physiology*, 1999, **86**, 1032-1039.